Princeton Plasma Physics Laboratory

PPPL-

PPPL-

PRINCETON
PLASMA PHYSICS
LABORATORY

Princeton Plasma Physics Laboratory
Report Disclaimers

Full Legal Disclaimer

PPPL Report Availability

Princeton Plasma Physics Laboratory:

http://www.pppl.gov/techreports.cfm

Office of Scientific and Technical Information (OSTI):

http://www.osti.gov/bridge

Related Links:

U.S. Department of Energy

Office of Scientific and Technical Information

Fusion Links

Disruptions, Disruptivity, and Safer Operating Windows in the High-β Spherical Torus NSTX

S.P. Gerhardt[1], R.E. Bell[1], A. Diallo[1], D. Gates[1], B.P. LeBlanc[1], J.E. Menard[1], D. Mueller[1], S.A. Sabbagh[2], V. Soukhanovskii[3], K. Tritz[4], H. Yuh[5]

1: Princeton Plasma Physics Laboratory, Princeton NJ, 08543 USA
2: Dept. of Applied Physics, Columbia University, New York NY, 10027 USA
3: Lawrence Livermore National Laboratory, Livermore, CA 94551, USA
4: The Johns Hopkins University, Baltimore, Maryland 21218, USA
5: Nova Photonics, Princeton NJ, 08540, USA

Abstract

This paper discusses disruption rates, disruption causes, and disruptivity statistics in the high-β_N National Spherical Torus Experiment (NSTX) [M. Ono, et al. Nuclear Fusion 40, 557 (2000)]. While the overall disruption rate is rather high, configurations with high β_N, moderate q*, strong boundary shaping, sufficient rotation, and broad pressure and current profiles are found to have the lowest disruptivity; active n=1 control further reduces the disruptivity. The disruptivity increases rapidly for q*<2.7, which is substantially above the ideal MHD current limit. In quiescent conditions, q_{min}>1.25 is generally acceptable for avoiding the onset of core rotating n=1 kink/tearing modes; when EPM and ELM disturbances are present, the required q_{min} for avoiding those modes is raised to ~1.5. The current ramp and early flat-top phase of the discharges are prone to n=1 core rotating modes locking to the wall, leading to a disruption. Small changes to the discharge fueling during this phase can often mitigate the rotation damping associated with these modes and eliminate the disruption. The largest stored energy disruptions are those that occur at high current when a plasma current rampdown is initiated incorrectly.

10 Sections
20 Figures
172 References

1: Introduction

Tokamaks and ST plasmas are prone to events known as disruptions, where a catastrophic loss of confinement leads to the rapid quench of the plasma current. The loss of energy confinement can lead to severe thermal loads on the plasma facing components [1-8], while the electromagnetic loads from the "current quench" [9-14] can lead to excessive mechanical loads [15]. The current quench can also lead to the generation of runaway electrons [6,7,16-21], which can result in catastrophic vessel and PFC damage [33]. Finally, if the control of the plasma vertical position [23-27] is lost, the plasma can drift up or down and come in contact with the vessel and PFCs; the "halo currents" [28-34] that are shared between those components and the plasma can lead to destructive forces [15]. Clearly, it is necessary to avoid these events.

The disruptive stability boundaries have traditionally been considered in terms of certain global parameters [35]. The limit on the plasma pressure is typically quoted in terms of the normalized β, defined as $\beta_N = aB_T \beta_T / I_P$ [36]. In the absence of a conducting wall, the value of β_N at which instabilities occur depends on the aspect ratio [37,38], boundary shape [39,40], and the shape of the current and pressure profiles [37,39,41]. When a conducting wall is present, image currents in the wall can provide a stabilizing effect, and the β_N limit can be higher. However, a new branch of the high-β kink instability can become unstable due the tendency of these currents to resistively dissipate. This instability, known as the resistive wall mode (RWM) [42,43], has been observed in both conventional aspect ratio tokamaks [44,45] and in STs [46-50]. It can stabilized by the presence of rotation and dissipation [42,43]. Alternatively, because the RWM growth rate is the comparatively slow L/R time of the relevant eddy current path in the conducting wall, direct feedback control using non-axisymmetric coils can be used [51,52].

The plasma current limit is typically written in terms of the edge safety factor q, often quoted at the flux surface containing 95% of the poloidal flux and denoted q_{95}, or as the cylindrical safety factor $q^* = \frac{\varepsilon\pi aB_T}{\mu_0 I_P}\left(1+\kappa^2\right)$. Ideal MHD calculations have shown q* is indeed a better aspect-ratio independent measure of the current limit [53], with values less than ~1.3 leading to ideal instability at any value of β_N. Early experiments in JET showed a clear disruptive boundary at q_{edge}=2 [54]; the lowest achievable q_{95} in PBW was ~2.2 [55]. More recent work in JET has shown a clear increase in disruptivity for q_{95}<2.5 [56]. In order to avoid these disruptions, ITER will operate at q_{95}≈3, corresponding to q* ≈2.5 (using I_P=15 MA, B_T=5.3 T, R_0=6.2 m, a=2.0 m, and κ=1.85 [57]). For the ST, Ref. [53] showed initial data that the low-q boundary may indeed occur at q* of ~1.3.

An additional disruptive stability limit is related to the plasma density [58-62]. This is normally captured by the Greenwald fraction [61], $f_{GW} = \bar{n}_e / n_{GW}$, where $\bar{n}_e$ is the line average density and $n_{GW} = \frac{I_P}{\pi a^2}$, with I_P in MA and n_{GW} in units of 10^{20} m^{-3}. In H-mode [63], exceeding the density limit typically results in a back transition to L-mode. In L-mode, exceeding the density limit typically results in a disruption. This disruption is

often associated with the cooling of the plasma edge and an increase in radiation [54], and there is evidence that formation of magnetic islands may play an important role in this process [62,64-66]

Finally, the formation of magnetic islands has been observed to limit the plasma β, even at densities significantly lower than the Greenwald limit. The most commonly considered form of such instabilities are the Neoclassical Tearing Modes (NTMs) [67-72], which occur in plasmas with a reasonably high bootstrap current fraction. These modes arise from the flattening of the temperature profile within a magnetic island: the resulting reduction in bootstrap current leads to a negative current perturbation, which reinforces the growth of the island for conventional positive tokamak magnetic shear. While $n \geq 2$ NTMs generally manifest themselves as a loss of confinement, $n=1$ NTMs can slow the plasma rotation and lock to the wall, often leading to disruption. Note that while the majority of NTM research has been conducted in conventional aspect ratio tokamaks, they have also been observed in the spherical torii NSTX [73,74] and MAST [75,76].

An important aspect of disruption avoidance is active control of MHD instabilities. The most basic example of this control is the regulation of the plasma vertical position with radial field feedback [25-27]; when this control is lost, the plasma can drift upwards or downwards, leading to a disruption known as a Vertical Displacement Event (VDE). More recently, active control has been demonstrated for both the slowly varying $n=1$ error field [77,78] and the rapidly growing $n=1$ the resistive wall mode [51,52,79-81]. Control of destabilized neoclassical tearing modes has been demonstrated with localized electron cyclotron current drive (ECCD) [72, 82-86], and NTMs have been avoided with so-called "preemptive ECCD" [87].

While these active mode stabilization techniques are critical, this paper addresses the more basic question of what operating regimes result in minimal disruptivity for a high-β spherical torus. These regimes would likely not eliminate the need for active stability control; rather, they may provide scenarios where active control have the best chance of eliminating disruptions. This is an important question in light of the wide range of operating points that have been suggested for next-step STs. For instance, in the context of the Fusion Nuclear Science Facility (FNSF) [88] mission, candidate spherical torus designs [89-95] have β_N values between 3.5 and 5.2 and q* values between 2.3 and 3.8. Clearly, empirical guidance on how these parameters impact disruptivity would be beneficial.

This paper describes i) global parameters that lead to minimal disruptivity in NSTX [96], and ii) some disruption causes and processes that have not been widely discussed in previous NSTX MHD publications. Section 2 discusses the analysis methods used in this paper. Section 3 describes some general statistics of NSTX disruptions. These include the disruption rate, the typical stored energies and plasma currents at the time of the disruption, and the stored energy and plasma current losses in the phase proceeding the disruptions. Section 4 describes the disruptivity statistics for neutral beam heated H-mode plasmas in NSTX; the disruptivity is studied as a function of single engineering or physics parameters, and in terms of pairs of relevant parameters. Section 5

discusses the impact of n=1 resistive wall mode control on the disruptivity. Section 6 discusses some of the phenomenology of disruptions during the early flat-top phase of the discharge. Section 7 discusses disruptions at the low-q* boundary. Section 8 discusses the role of q_{min} evolving towards unity in determining the onset of often disruptive core n=1 modes, while Section 9 describes the phenomenology of very high stored energy disruptions in NSTX. Section 10 provides a summary of these results.

NSTX is a medium size spherical torus located at Princeton Plasma Physics Laboratory. The major radius of typical plasmas is R_0=0.85 m, with aspect ratios R_0/a=1.35 to 1.55. The plasma currents are typically in the range 600<I_P [kA]<1300, with toroidal fields between 0.35 T and 0.55 T. Neutral beam heating with powers up to 7 MW, oriented parallel to the plasma current, is used for most high-performance plasmas, [97] and can be used for β_N control [98]. High-harmonic fast wave heating at 30 MHz with powers up to ~6 MW is also available [99].

2: Analysis Methods

In this paper, the correlation of selected parameters with increasing disruptivity will be addressed. The definitions of these parameters, and the analysis methods utilized, are the subjects of this section.

A key question to address is the definition of disruption onset. Fig. 1 shows the I_P and β_P waveforms for three different disruptions; β_P is chosen as a surrogate for stored energy at largely fixed I_P, and is defined as $\beta_P = \dfrac{2\mu_0 \langle P \rangle}{B_P^2}$, with $\langle P \rangle$ the volume average pressure, the poloidal field defined as $B_P = \dfrac{\mu_0 I_P}{l_P}$, and l_P the poloidal circumference. Two times are indicated by vertical lines in each frame: the time of the current quench (t_{quench}) in red, and the time of the first negative I_P deviation (t_{IpDev}) in blue. The time of the current quench is clearly relevant for disruption physics studies, but it is also clear that in many cases, the plasma energy and profiles have evolved considerably from those at the time of the first I_P deviations. In general, we will find that t_{IpDev} is the better time to consider when doing disruptivity analysis, as it is more closely related to the time when the stability boundaries are crossed that precipitate the disruption process.

Fig. 2 shows a histogram of t_{quench}-t_{IpDev}. It can be seen that in most cases the I_P deviation time precedes the current quench by between 0 and 0.1 s. There are a few cases where the t_{IpDev} comes after t_{quench}; these correspond to cases where there is an I_P spike of fairly long duration but no pre-disruption current loss; t_{quench} is defined by the beginning of the spike, and is thus before the first negative deviations.
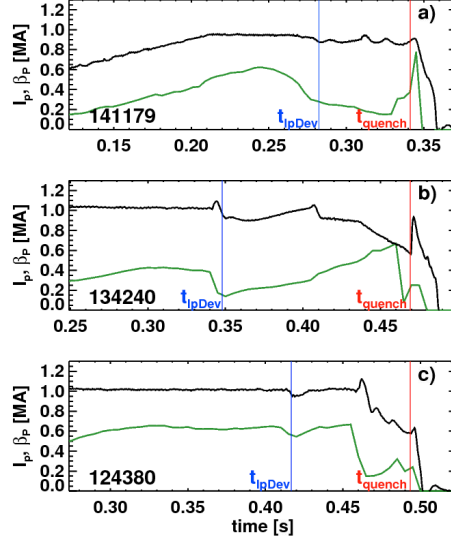
4

Fig.1: Evolution of the plasma current (black) and poloidal β (green) for three disrupting discharges. See text for further details, and note the large current loss before the final current quench at t=t_{quench} in frames b) and c).
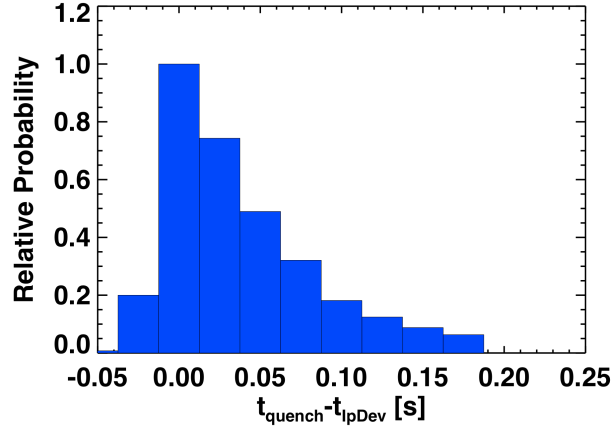
Fig.2: Histogram of t_{quench}-t_{IpDev}, the time between the first meaningful negative deviation of I_P and the time of the current quench.

Two independent executions of the equilibrium reconstruction code EFIT [100] occur after every NSTX discharge. The EFIT01 [101] is constrained by measurements of the plasma current, coil currents, estimates of the vessel currents, and poloidal field and flux measurements at discreet points along the plasma boundary. The EFIT02 [49] reconstruction is constrained by those measurements, plus the plasma diamagnetism and a loose constraint on the pressure profile from the density and temperature measured by multi-point Thomson scattering (MPTS) [102]. The EFIT02 generally produces better reconstructions and is present for the vast majority of NSTX discharges; this study only uses discharges that have this reconstruction available.

We have sampled data from every discharge in the NSTX database since 2005, with sampling time of 0.0333 seconds. This time matches the minimum confinement time of a typical H-mode NSTX discharge (see Fig. 6 of Ref. [103]), but is longer than the

typical MPTS update times or times between EFIT reconstructions. Quantities recorded on this timebase include many equilibrium properties from EFIT, the heating power from the neutral beam and High Harmonic fast wave heating systems, the electron temperature and density from a multi-point Thomson scattering diagnostics, the toroidal rotation as measured by the charge exchange spectroscopy (CHERS) diagnostic [104], and the total radiated power from an array of bolometers.

In addition, the database records as best available whether there were characteristics of a discharge which make it more or less prone to disrupt. For instance, any faults reported by the computer that controls the poloidal & toroidal field coils are recorded. The amplitude and toroidal mode number of any magnetic braking [105-110] applied to the plasma are recorded, as are the status of n=1 RWM control [52, 109,111], n=1 dynamic error field correction [78], and n=3 error field correction [112]. Also recorded are any non-standard techniques applied to the plasma, including vertical jogs for ELM pacing [113], pulsed 3D fields for ELM pacing [114-116], or isoflux [117,118] control of the divertor X- and strike-points [119,120]; these are not necessary disruptive techniques, but a large fraction of the discharges utilizing them were for development, when the disruption rate was higher. Finally, the database records if the discharge was taken during a phase with "good conditions", or during a phase of machine commissioning at the beginning of the run or with known bad vacuum or PFC conditions.

With regard to the tendency of the plasma to disrupt, there are two quantities that can be considered: the disruptivity and the disruption rate. The disruptivity is defined as the number of disruptions that occur when the plasma is in a particular parameter space, divided by the total duration that the plasma is in that state [56]. This disruptivity is thus related to the state of the plasma at any particular time, and will be studied in the context of NSTX data in Sect. 4 & 5. The disruption rate, on the other hand, is simply the fraction of discharges that disrupt during some part of the discharge; the disruption rate in NSTX will be briefly summarized in Sect. 3. Of the two measures, the disruptivity is likely to be more closely related to the physics that determines the operating space.

3: Disruption Statistics and Phenomenology in NSTX

Some basic statistics regarding the NSTX disruption rate are shown in Fig. 3. Fig 3a) shows the total number of discharges under consideration, for the 2005-2010 run campaigns. The green points in this figure show that starting in 2008, there was a dramatic increase in the total number of discharges. This is due to the use of lithium conditioning of the plasma facing components [121,122] that allows the time between discharges to be reduced to 10 minutes, without the between-shot Helium glow discharge cleaning (GDC) that was typical of previous NSTX operations and mandated a 15-20 minute cycle time. The magenta triangles show the total of number of discharges taken during phases with good conditions, and with no ELM pacing or magnetic braking. These generally track the total number of discharges, except in the 2009 campaign. Residual lithium carbonate left inside the vessel from the previous run campaign compromised the beginning of the 2009 campaign, and the problem was only remedied by a series of noble

gas glow-discharge phases, followed by helium GDC and conditioning with fresh lithium.
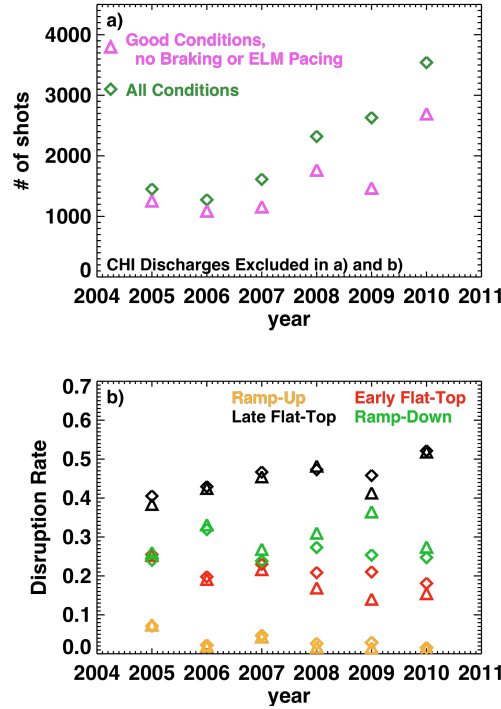

Fig. 3: a) The number of discharges and b) the disruption rate, for NSTX, sorted by year. The diamonds correspond to all discharges, while the triangles correspond to discharges where the machine conditions were nominally good and neither ELM pacing nor magnetic braking were used.

The disruption rate as a function of year is shown in Fig. 3b, divided into four categories. The yellow points correspond to disruptions during the plasma current ramp-up. These are a very small fraction of the total number of disruptions, and their frequency has generally decreased in more recent campaigns.

The red points, labeled "Early Flat-Top", correspond to disruptions that occur within 0.25 s of the start of the I_P flat top (SoFT). During the first 0.25 s after SoFT, the q=4,3, and 2 surfaces enter the plasma as the current penetrates to the core. As will be discussed in more detail in Section 6, instabilities at these rational surfaces often slow the plasma rotation and lock to the wall, leading to a disruption. There has been a modest reduction in disruptions during this early phase of the discharge during recent campaigns.

Disruptions during the later flat top are shown as black points in Fig. 2b). These cases correspond to disruptions that occur between 0.25 s after the SoFT, and the end of flat-top (EoFT), which is defined by either the pre-programmed ramp-down of the plasma current or the ohmic heating coil reaching its current limit. The discharge characteristics leading to disruptions in this phase of the discharge have been well documented in previous NSTX publications, and include resistive wall modes [46,47,49,52,109,111] sometimes caused by diminished rotation due to uncorrected error fields [78,112], n=1

kink/tearing modes that lock to the wall [73,103,123-125], loss of vertical position control, and H->L back transitions driven by plasma-wall gaps becoming to small or insufficient input power. The fraction of discharges disrupting during the flat-top has increased slightly in recent years.

Finally, disruptions during the ramp-down are indicated in green. Note that NSTX did not have any automated, event-based stored energy and current ramp-down algorithm. Hence, this category include cases where the plasma current is deliberately ramped down, though typically without any ramp-down of the beam power or modifications to the shaping. It also includes the many cases where the solenoid current limit is reached during the disruption-free flat-top period. The rapid reversal of the loop voltage as the solenoid current returns to zero often results in disruption, which is classified here as having occurred during the ramp-down. In any case, disruptions during this phase of the discharge have been fairly constant over the recent run campaigns. It is likely that if more careful discharge termination strategies were developed, this class of disruption could be reduced in frequency.

We also note the apparent increase in the rampdown disruption rate during the 2009 campaign. This can be attributed to the reduced rate of early and late flat-top disruptions during that campaign. More discharges lasted to the ramp-down phase during that campaign, increasing the disruption count during that phase. Unfortunately, the positive disruptivity trends in 2009 were not maintained for the 2010 campaign, likely due to operational complexity associated with the Liquid Lithium Divertor [126] modules.

Overall, it is clear that the disruption rate in NSTX is quite high, with the majority of shots disrupting during the pre-programmed I_P flat-top, and a small fraction of discharges lasting through the ramp-down without disruption. We wish to note, however, that this large disruption rate has not been the barrier to scientific progress that might at first be assumed. Disruptions in NSTX generally have a negligible effect on the performance of the subsequent plasma, so that the rampdown disruptions have essentially no impact on the research program. Some of the late flat-top disruptions interfere with the goals of the discharge, but there is quite often sufficient duration previous to the disruptions for the physics goals of the discharge to be met. Only the early flat-top disruptions are uniformly detrimental to the physics program.

Having established the frequency with which disruptions occur, we now focus on some general characteristics of these disruptions. Fig. 4a) illustrates a histogram the stored energy at the time t_{quench}, and Fig. 4b) shows a histogram of current quench rates. The quench rate is defined using the "80-20" definition [11] $QR_{(80-20)} = -\dfrac{.6 * I_{PD}}{t_{20} - t_{80}}$, where I_{PD} is the plasma current at t_{quench} and t_{20} and t_{80} are the times when the plasma current has decayed to 20% and 80% of I_{PD}. These two quantities reflect the mechanical [15] and thermal loading [3] due to the disruptions.
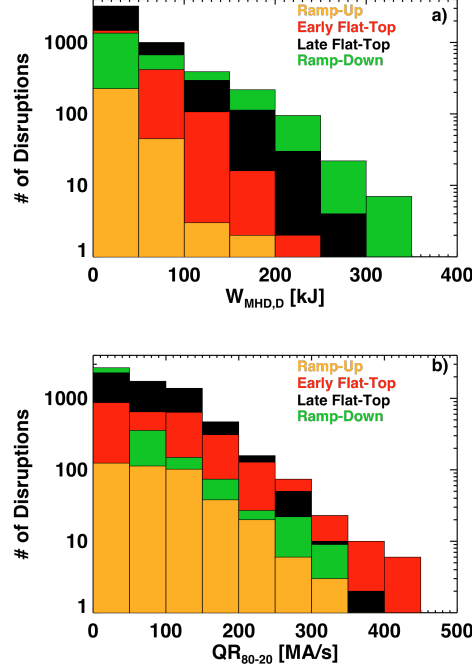
Fig. 4: Histograms of a) the pre-disruption stored energy and b) the current quench rates for NSTX disruptions since 2005

With regard to stored energies in Fig. 4a), we see that disruptions during the I_P ramp-up and early flat-top typically do not have large stored energy at times just preceding the current quench. This is not a surprise, in that the discharges have not had sufficient time to reach high values of W_{MHD} before disrupting. On the other hand the largest stored energies at the time of the current quench are in the range of 350 kJ, and are clearly associated with disruptions during the I_P ramp down; the phenomenology of these disruptions will be discussed in detail in section 9. Disruptions during the I_P flat-top have maximum stored energy in the range of 250 kJ.

Fig. 4b) shows that fast quenches are unlikely during the disruption rampdown and later flat-top. Rather the highest quench rates tend to occur during the early flat top. Note that current quench rates up to 1 GA/s have been observed in NSTX during the earlier operation of NSTX [12]; however, quench rates that high have not been observed in the more recent run campaigns that contribute data to the present analysis.
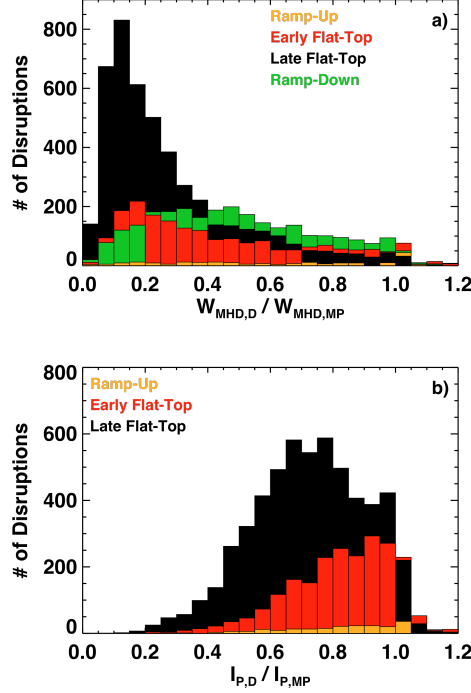
Fig. 5: Histograms of the pre-disruption loss fractions of the a) stored energy, and b) plasma current, for disruptions since the 2005 run campaign.

In addition to the quench rate and stored energy, it is interesting to consider how much plasma current and stored energy are lost during the pre-disruption phase, as these losses will tend to mitigate the effects of the disruptions. These quantities are shown in Fig. 5, where the data is again sorted by the phase of the discharge during which the disruption occurs.

With regard to the stored energy loss, we see that large stored energy losses are the norm for discharges disrupting during the flat top, and especially during the later flat-top. This is the reason why the maximum disruption stored energy during the flat-top is ~250 kJ, despite the maximum stored energy in NSTX being ~460 kJ [103]. Ramp-up disruptions tend to have a smaller fractional stored energy drop, but also tend to have fairly low stored energy. On the other hand, the stored energy loss for rampdown disruptions is more evenly distributed, with many examples showing no pre-disruption energy loss. An example disruption in this category will be discussed in Section 9.

With regard to the pre-disruption current loss, Fig. 5b) illustrates results fairly similar to the trends in stored energy. The plasma current loss for disruptions during the ramp-up or early flat-top can be fairly small, with the peak in the histogram occurring at or near $I_{P,D}/I_{P,MP}$ unity, but a large tail to small values of $I_{P,D}/I_{P,MP}$; see Fig. 1 for examples with large current loss. Disruptions during the later flat-top tend to have a larger loss of current before the current quench.

Finally, we note that the while this discussion has focused on the current quench and stored energy loss, runaway electrons and halo currents can also cause damage to the

tokamak plant during a disruption. Halo currents in NSTX have been discussed in Ref. [34], and in the spherical torus MAST in Ref. [31]. Disruption-generated runway electrons have not been observed in NSTX.

4: Disruptivity analysis for NB heated H-mode plasmas.

This section examines the disruptivity in various portions of parameter space. Recall that the database includes all NSTX discharges, sampled 30 times per second. However, the data utilized in the analysis in this section does not include all of these samples. Constraints applied to the data in this section include:

- The discharge must have at least 0.6 MJ of neutral beam energy injected, and at most 2.5 kJ of HHFW power. This constraint effectively restricts the database to dominantly neutral beam heated discharges. Note that most concepts for next-step ST devices utilize dominantly NB heating (in addition to fusion power), and so this data filter appears quite appropriate.
- Discharges with CHI plasma initiation are excluded.
- Deliberate VDEs and discharges with PF-coil power supply faults are excluded.
- The confinement at each sample, defined by the parameter H_{89} [127], must exceed 1.2. This constraint serves to localize the data to the high-performance phase of the discharge, and excludes samples during the low-confinement phase that precedes most disruptions.
- The magnetic-axis location at each sample must be within 15 cm of the vessel midplane. This excludes samples during the vertical motion of a VDE.
- Only discharges during phases of a run campaign with nominally good PFC conditions are included.
- Samples during which magnetic braking is applied are excluded unless otherwise stated.

4.1) 1D Disruptivity analysis

Fig. 6 shows the disruptivity statistics as a function of four primary engineering parameters in NSTX operation: a) the plasma current, b) the toroidal field, and c) the total input power, and d) the Greenwald fraction. The upper blue histogram in each frame shows the disruptivity itself. The lower histogram in red shows the negative logarithm of the distribution of all samples, in order to clearly portray the distribution of data.

Fig. 6a shows that the disruptivity has a minimum in the range of plasma currents 0.7 MA<I_P<1.0 MA. Above 1.0 MA, the edge and central safety factors tends to drop toward values that precipitate disruption, as will be discussed in more detail below. When the disruptivity is plotted against toroidal field, we see that the disruptivity is fairly constant from 0.35 T through 0.45 T. Higher toroidal fields result in prohibitively short plasma durations due to heating limits on the TF coil itself, and so operations in this regime is typically reserved for non-standard operating conditions. Examples of such non-standard conditions that contribute to a higher disruption rate include experiments designed to maximize the non-inductive current fraction at very high elongation & β_N, or

L-H threshold experiments. Thus, the observed increase in disruptivity at higher toroidal field is likely a result of the NSTX research program. Fig. 6c) shows that there is a significant reduction in the disruptivity as the heating power is increased, an apparently paradoxical result that will be discussed in greater detail below. Finally, Fig 6d) indicates a broad region of minimal disruptivity for Greenwald fractions of $0.35 < f_{GW} < 1.0$, indicating that the allowable density operating range is quite broad. The increase in disruptivity above $f_{GW} = 1$ may be related to the density limit. However, the phenomenology of those disruptions has not been verified as being similar to that of density limit disruptions in conventional aspect ratio tokamaks.
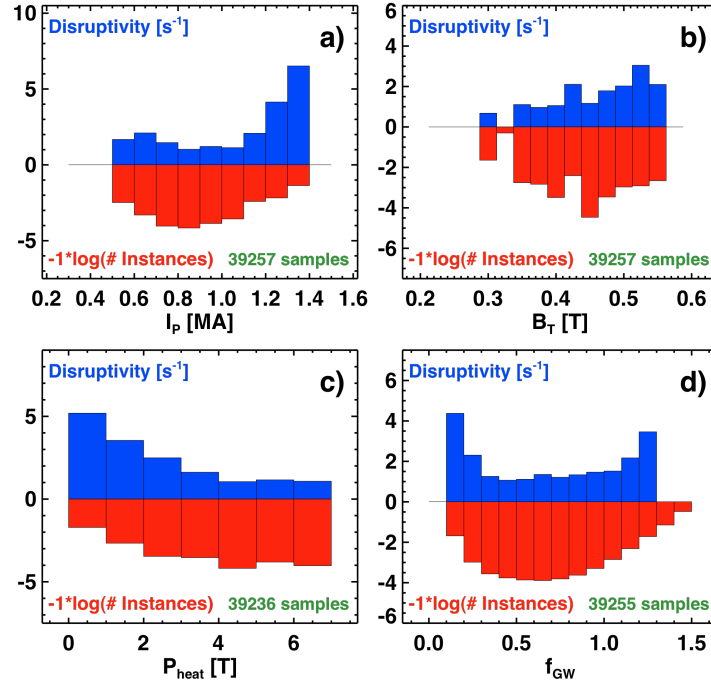

Fig.6: Histograms of the disruptivity (blue) and sample distribution (red) vs. the engineering parameters a) I_P, b) B_T, c) P_{heat}, and the d) Greenwald fraction f_{GW}.

This same analysis is repeated in Fig. 7, but for physics parameters thought to be indicative of tokamak and ST operational boundaries. Fig. 7a) shows the disruptivity as a function of β_N. Interestingly, there is no clear increase in disruptivity at the highest value of β_N. Indeed, the disruptivity tends to be higher for $\beta_N < 4$ than for $\beta_N > 4$, though the effect is not dramatic. Of course, there is a β limit in NSTX. However, it cannot be easily captured by a single value of β_N, and it is clear that other parameters impact this limit.
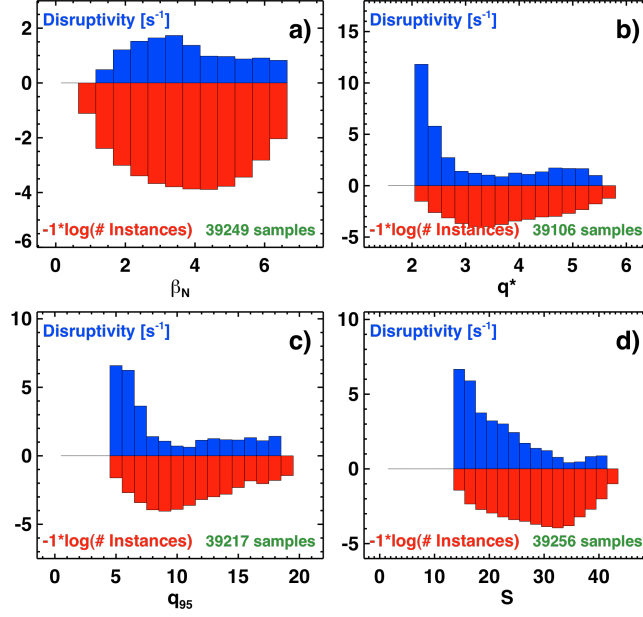
Fig.7:Disruptivity as a function of a) β_N, b) q^*, c) q_{95} and the d) shape parameter S.

In contrast, there is a clear increase in disruptivity for lower values of the edge safety factor. This is illustrated in Figs. 7b) and 7c), where there is a dramatic increase in disruptivity for $q^* < \sim 2.7$ or $q_{95} < \sim 7.5$. This low-q disruptivity boundary will be discussed in more detail in Section 7.

As indicated in the introduction and implied by the discussion of Figs. 7b) and 7c), the plasma boundary shaping plays a strong role in determining the disruptivity. We can combine the various shaping effects (aspect ratio A, elongation κ, triangularity δ) in a single parameter known as the shape factor S [128], which depends on the shape moments roughly as $S = \dfrac{q_{95} I_P}{a B_T} \propto \varepsilon \left(1 + \kappa^2\right) f\left(\kappa, \delta, \varepsilon, ...\right)$. To provide some perspective on this quantity, Fig. 8 shows two plasma boundaries. The left boundary has the highest elongation compatible with filling the vacuum chamber while leaving reasonable plasma-wall gaps, and has a shape factor of 37. Note that the outer boundary is also quite conformal to the passive plates, resulting in good coupling and wall stabilization. This shape is indicative of that used for the highest performance plasmas in the later NSTX run campaigns. The case on the right has both lower elongation and triangularity, and results in a shape factor of ~20. It is also more poorly matched to the outer contour defined by the passive plates. Returning to frame 7d), we see that the disruptivity drops rapidly as the shape factor is increased, and has a minima at shape factors of 35-40. This result reinforces the role of strong shaping in facilitating high performance operations.
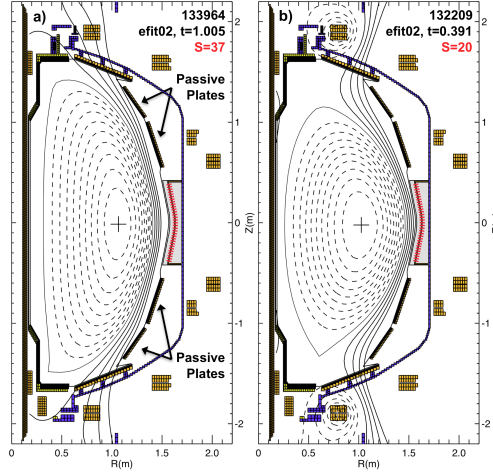
Fig.8: Example plasma boundaries with extreme values of the shape factor S. Frame a) shows a strongly shaped plasma with S=37, while frame b) shows a weakly shaped plasma with S=20.

The plasma stability is also a function of internal profile shapes, and Fig. 9 shows that these dependencies are reflected in the disruptivity statistics. The first quantity under consideration is the pressure peaking factor, defined as the central pressure normalized to the volume average pressure ($F_P = p_0/<p>$). It is well documented from theory [41] and experiments at conventional [39,129-132] and low [46,47,103,133] aspect ratio that increases in the pressure peaking factor have a deleterious effect on the global stability. Fig 9a) shows that the disruptivity is minimized for the lowest values of the pressure peaking factor, and increases up to peaking factors of about 3. The disruptivity then stays high through $F_P = 5$. There is some reduction in disruptivity at very high pressure peaking. This region is dominated by low-β_N L-mode time-slices, often early in the I_P flat-top before the L->H transition; these equilibria are not of interest as the target scenario for future ST development.

We see a similar trend in the disruptivity as a function of the internal inductance, defined as $l_i = l_i(1) = l_P^2 \iiint B_P^2 dV \Big/ V\left(\mu_0 I_P\right)^2$, where V is the volume of the plasma; this parameters is indicative of the current profile shape, with high values of l_i indicating that the current profile is more strongly peaked on axis. The minimum disurptivity occurs at low values of l_i, and increases dramatically as l_i increases. Simplistically speaking, there are at least three reasons for this trend. Firstly, the efficacy of the plasma shape and vertical position control increases when l_i is lowered, since the plasma current is then closer to the coils. Secondly, moving more current closer to the edge increases the coupling to the wall and improves the global n=1 stability in the wall stabilized regime. Third, equilibrium and current drive calculations show that increased l_i is often associated with increases in the pressure peaking [34], which is independently associated with increases in disruptivity.

The no-wall stability limit is often quoted as being proportional to value of l_i, with ratios between 2.5 and 4 indicative of the stability limit at conventional aspect ratio.

However, as can be expected from Figs. 7a) and 9c) and illustrated in Fig. 9c), the disruptivity in NSTX is generally lowest at high values of β_N/l_i . This is the result that should be expected when operating in the wall-stabilized regime, and in scenarios where maintaining elevated q_{min} is a requirement for disruption avoidance (see Sect. 8).
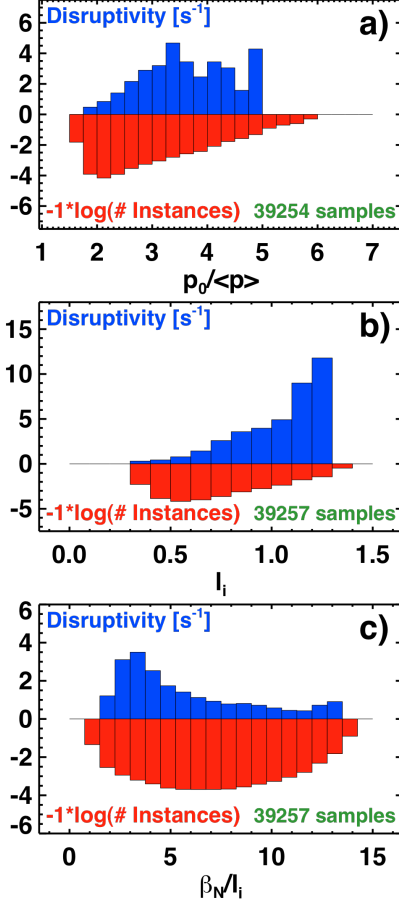

Fig 9: Disruptivity as a function of a) the pressure peaking factor, b) the internal inductance, and c) β_N/l_i.

Finally, we consider the disruptivity as a function of rotation in Fig. 10. For this analysis, we consider the rotation in both the plasma core and the midradius, and we include samples where magnetic braking was applied to the plasma. Here, the core is defined as the average of CHERS channels 4 through 7 spanning R=0.99 to 1.09 m, while the midradius is defined as the average of the CHERS channels 16-20 spanning R=1.27-1.34m; these midradius chords are in the vicinity of the q=2 surface for typical NSTX NBI heated discharges.

Figs. 10a) and 10b) indicate that the disruptivity is independent of rotation over a wide range. However, we find a significant increase in disruptivity for $F_{T,core}<\sim6$ kHz, or $F_{T,mid-radius}<\sim3$ kHz. One reason for this trend is the tendency for rotating core n=1 modes that initiate at higher plasma rotation to slow and ultimately lock the plasma. This will be observed in Fig. 14 of this paper for modes early in the I_P flat-top and Fig. 15 for modes in the later phase of the discharge, or for later flat-top modes as described in Ref.

15

[124,125] and section 6.3 of Ref. [103]. The other reason for increased disruptivity at low rotation is related to the resistive wall mode.
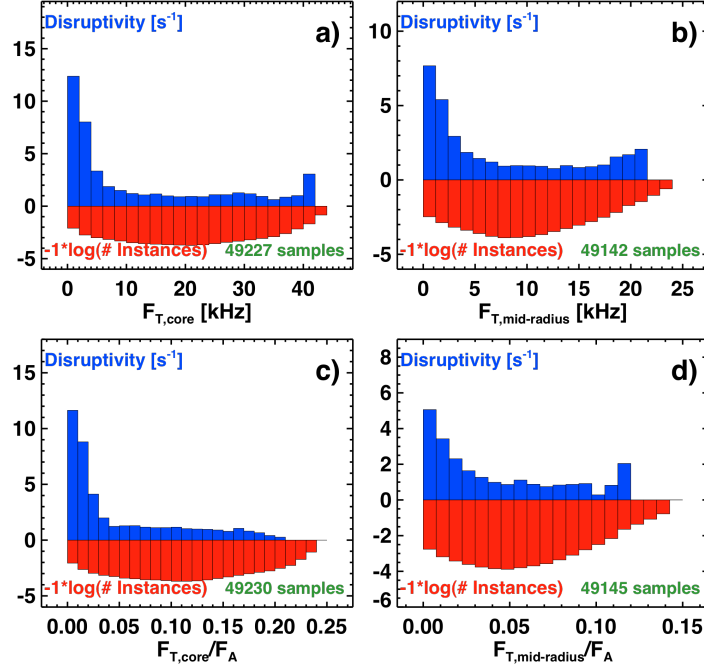

Fig.10: Disruptivity plotted against a) the core and b) mid-radius rotation. Frames c) and d) show the same data, normalized to the Alfven frequency. See text for additional details.

Various papers from NSTX, DIII-D, and JT-60 have reported a threshold for resistive wall mode onset in terms of the rotation normalized to the Alfven frequency [48,80,135,136]. For instance, in looking at early NSTX data, Ref. [48] reported that the threshold was a profile quantity, and that stability was indicated by the criterion $V_\phi \tau_A > 1/4q^2$. Using this as guidance, the rotation data is normalized by $F_A = V_A / 2\pi R_0$ (with $V_A = |B_0| / \sqrt{2\mu_0 \overline{n}_e m_P}$). Here, $|B_0|$ is the central vacuum toroidal field and $\overline{n}_e$ is the line-average density. The disruptivity is plotted as a function of normalized rotation in Fig. 10 c) and d). We find that, in an approximate sense, the disruptivity increases for $F_{T,core}/F_A < 0.03$ or $F_{T,mid-radius}/F_A < 0.02$.

4.2) 2D Disruptivity analysis

In this section, we consider the 2D plots of the disruptivity vs. β_N and an additional parameter, with the goal of determining additional correlations not present in the 1D histograms of section 4.1.

Fig. 11a) shows the disruptivity as a function of β_N and q*. It is clear that operation at low q* increases the likelihood of disruption for essentially all β_N, but that

this likelihood is largely independent of q* for q*>~3. This plot also shows that there is a broad region of low disruptivity in the vicinity of β_N=6 and q*=3.5. The same disruptivity data is plotted against β_N and shape factor S in Fig. 1b). This figure shows a strong region of minimum disruptivity at high β_N and strong shaping.
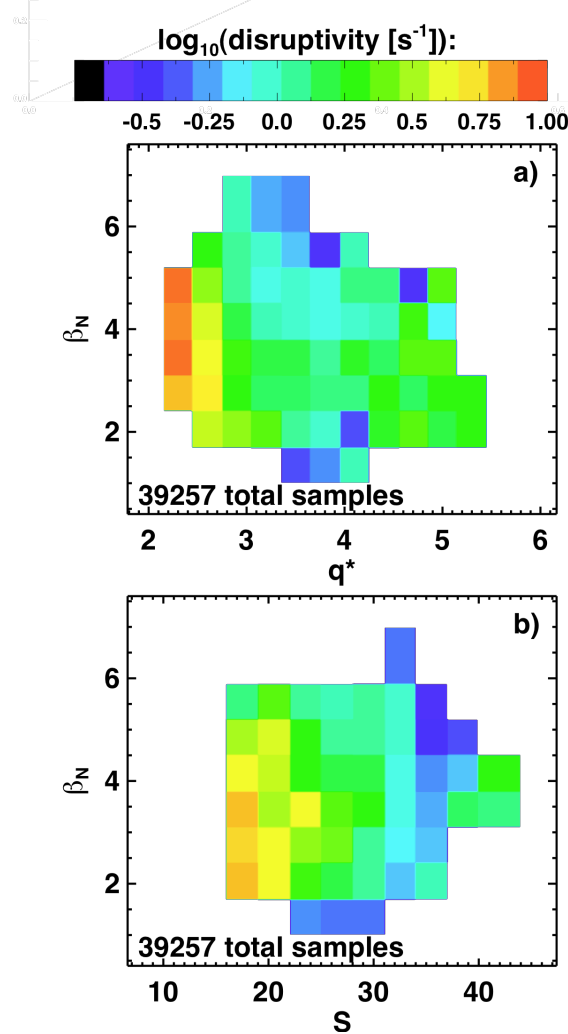
Fig. 11: Disruptivity as a function of β_N and a) the cylindrical safety factor q*, or b) the shape factor S.

The disruptivity is plotted as a function of β_N and profile parameters in Fig. 12. This figure shows that the disruptivity is comparatively low for all β_N when F_P (Fig 12a)) and l_i (Fig. 12b)) are sufficiently low. In both cases, there is in increase in disruptivity when the profiles become more peaked (larger values of $p_0/\langle p \rangle$ or l_i), and that the highest disruptivity occurs with peaked profiles and higher β_N. Note that there is a small region of reduced disruptivity at higher F_P=$p_0/\langle p \rangle$, but low β_N. This region explains why the 1-D disruptivity in Fig. 9a) does not increase monotonically with F_P.

Fig. 12: Disruptivity as a function of β_N and a) the pressure peaking factor, or b) the internal inductance.
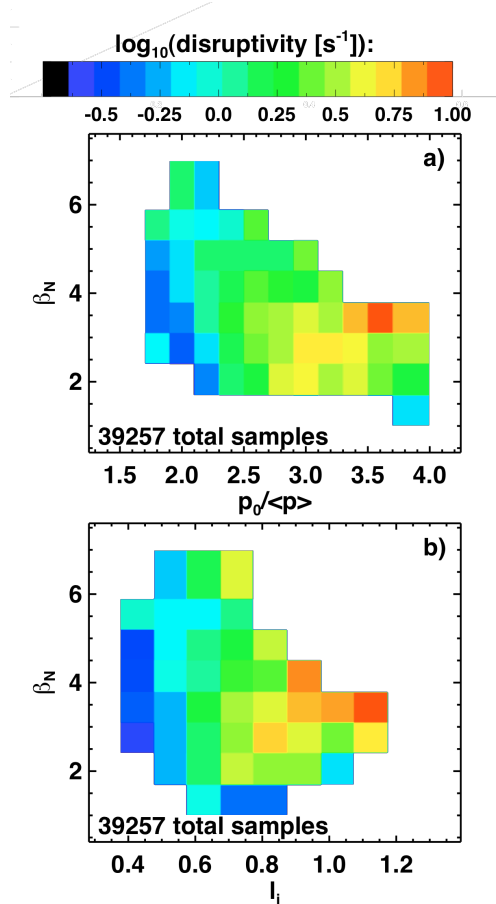
4.3) Discussion of Disruptivity

The figures in this section demonstrate that a window of minimal disruptivity exists at high-β_N with strong shaping and broad pressure and current profiles. However, the data in Fig. 3 indicates that a large fraction of discharges disrupt during the later flat-top, during the high-β phase. The reason for this is that the optimal profiles and boundary shape were typically not maintainable in NSTX. Reasons for deviation from the optimal operating points include:

- *Current diffusion:* Many NSTX discharges had current profiles that evolve through the I_P flat-top period, with q_{min} approaching 1. When this occurs, rotating n=1 kink/tearing instabilities often onset [103,123-125]. These instabilities always result in significant confinement degradation, and often lock to the wall, leading to disruption. These modes will be discussed in greater detail in section 8.

- *Kinetic profile evolution*: The density in NSTX discharges typically ramps continuously through the discharge. In discharges without lithium conditioning this evolution is due to an increase in the deuterium concentration. This density rise often resulted in MARFE formation, with a resulting degradation of the edge

pedestal. In ELM-free conditions [137-139] created by lithium conditioning, the accumulation of carbon results in an increase in the electron density. MARFE formation was typically eliminated in these cases [140]. However, the steady impurity accumulation in those scenarios resulted in large increases in Z_{eff} and radiated power, both of which eventually result in a deviation from the desired high performance operating point.

- *Actuator or plasma control failure*: NSTX high-performance H-mode discharges are extremely sensitive to the loss of auxiliary power input, with H->L back transitions and disruption typically following within 100 ms of sudden termination of the neutral beam power. Similarly, boundary shape control errors that result in plasma-wall gaps becoming too small often result in H->L back transition and disruption. Note that most high-elongation, high-performance discharges in NSTX were run without closed-loop X-point height control. This often resulted in the X-point approaching the divertor floor late in the discharge due to uncompensated leakage flux from the Ohmic solenoid coil.

5: Impact of n=1 control on the disruptivity at high-β_N.

The discussion above has indicated that with proper shaping of the plasma boundaries and broad pressure & current profiles, it is possible to significantly reduce the disruptivity at high-β_N. An additional mechanism for disruptivity reduction is the proper correction of non-axisymmetric error fields and feedback on resistive wall modes.
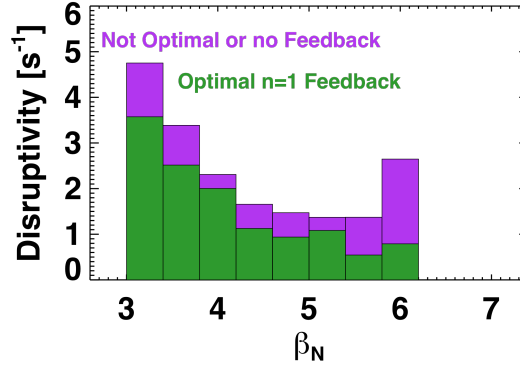
Fig. 13: Disruptivity as a function of β_N, sorted by whether feedback-based n=1 control was applied. This data is for the 2007-2009 experimental campaigns. See text for additional details.

During experiments in 2007 and 2008, a general recipe for n=1 dynamic error field correction and RWM feedback was determined via two different methods. In the first method [78], a small n=1 error field was applied, which was then amplified by the high-β plasma, leading to rotation damping and RWM driven disruption. The feedback system was then used to apply an n=1 field proportional to the detected plasma amplified n=1 perturbation (the direct coupling of the error field coils to the sensors was removed

before the feedback field was determined). There was a preferred phase between the detected field and the applied n=1 field which resulted in the near cancelation of the original pre-programmed n=1 currents and an extension of the pulse length. This feedback phase and associated feedback amplitude were then used for dynamic error field correction in subsequent discharges without the seed n=1 field.

In related experiments, rapidly growing resistive wall modes were generated without the use of applied n=1 fields, though n=3 magnetic braking was sometimes used. The n=1 feedback phase and amplitude were then scanned in order to determine the parameters that resulted in best suppression of the rapidly growing mode [Sabbagh 2010]. The amplitude and phase so determined were quite similar to that determined from the dynamic error field correction experiments, as expected given that the plasma amplified error field should have the characteristics of the marginally stable resistive wall mode [135,141,142].

With this background, Fig. 13 shows the disruptivity as a function of β_N, for discharges with the optimal n=1 error field correction, and for discharges which do not have such correction. This figure includes data from the 2007-2009 run campaigns, during which there was considerable operation both with and without n=1 control. Data from the 2010 campaign, which used n=1 control for virtually all beam heated discharges and had a major change to the plasma facing components in the form of the Liquid Lithium Divertor, are excluded from the figure.

It is clear that the use of n=1 control improved the discharges; in particular, for any given β_N, the disruptivity was reduced. We note that the n=1 control system is not expected to eliminate all disruption causes. For instance, VDEs or the disruptions following H-> L back transitions are not expected to be impacted by the use of n=1 control. With this caveat, it is clear that the n=1 control system was quite useful in reducing disruptivity, and it appears likely that future STs should have some capability for at least dynamic error field correction, if not fast feedback.

6: Phenomenology of early-flat-top disruptions.

It was noted in section 3 that approximately 20% of discharges disrupt during the early flat-top period, when the various rational surfaces are still entering the plasma. A spectrogram and example waveforms for a common disruption type in this category is shown in Fig. 14. The spectrogram and toroidal mode decomposition of dB/dt in Fig. 14a) shows a series of n=1 and n=2 chirping instabilities before t=0.2. An n=1 mode at approximately 15 kHz forms at about 0.22 seconds, but vanishes by t=0.25 seconds. A second larger n=1 mode is formed at about t=0.25 seconds. The frequency of this mode decreases continuously, ultimately dropping to zero rotation. Analysis of soft X-ray, reflectometer, and magnetics data indicates that these low frequency modes originate as kink instabilities [143].
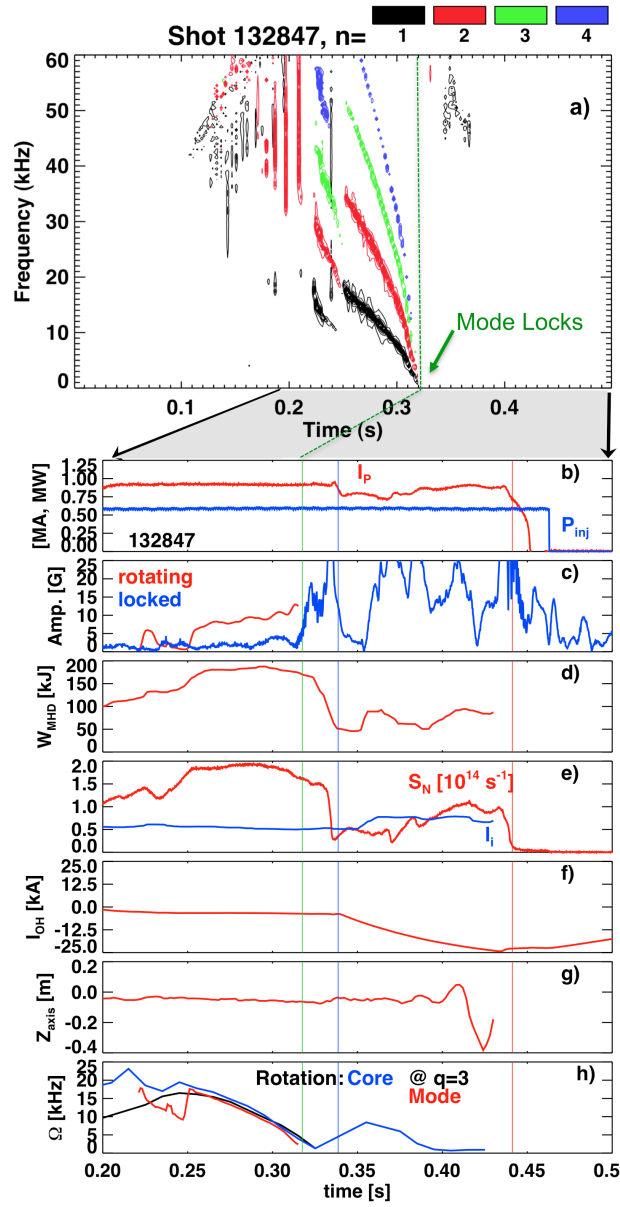
Fig. 14: a) Spectrogram and toroidal mode decomposition for a discharge that disrupts in the early flat-top due to MHD modes locking to the wall. Following are waveforms for b) the plasma current and heating power, c) the rotating and stationary mode amplitude, d) the plasma stored energy, e) the neutron emission and internal inductance, f) the solenoid current evolution, g) the plasma vertical position, and h) the rotation frequency in the core and at q=3, as well as the mode rotation frequency. Note that the time-scales are different in the top frame compared to the other frames.

The waveforms for this discharge are shown in the bottom time traces of Fig. 14. Fig 14b) shows the plasma current and heating power. The times t_{quench} and t_{IpDev} are indicated as vertical lines, and indicate that there is a long period between the first I_P deviation and the current quench. Fig. 14c) shows the signatures of the MHD activity that precipitate this disruption. The red curve shows the amplitude of the rotating mode that eventually locks. This signal vanishes when the mode locks at t=0.32 s (indicated by a

green vertical line), and is replaced by the rapidly growing locked n=1 mode signature in blue. The stored energy in Fig. 14d) begins to drop rapidly once the stationary mode begins to grow; this is partially due to an H-L back-transition that occurs at t= 0.325, resulting in the loss of the edge pedestal, as well as degradation in the core confinement. We also see in Fig. 14e) the very rapid loss of neutron emission. Because the neutron rate is largely proportional to the fast ion density in NSTX [144], this rapid drop is indicative of a rapid loss of fast ions.

The mode locking and severe confinement degradation is followed by a new set of plasma dynamics. Fig. 14e) shows that the internal inductance increases significantly in this L-mode phase, as the inductive currents, which can rather rapidly penetrate to the axis, become dominant in the low-β plasmas. This is reflected in the much more rapid ramp of the solenoid current I_{OH} after the mode locks; the solenoid current eventually reaches its current limit of -24 kA, and begins to return to zero. The large disturbances and increased internal inductance result in rapidly growing vertical motion in Fig. 14g), which the vertical position control system is unable to stabilize. Discharges of this type typically disrupt when either i) the loop voltage is reversed when the solenoid current begins to ramp to zero, or ii) uncontrolled vertical motion result in the plasma being driven into the divertor; in the present case, it appears that the vertical motion precipitates the final disruption. Finally, note that while this discharge comes from an early flat-top disruption, the events are generally representative of the sequence of RWM or mode-lock disruptions at higher β_N later in the flat-top.

Additional dynamics of the locking itself are shown in Fig 14h). The core plasma rotation is indicated in blue, while the rotation frequency at the q=3 surface is shown in black. Initially, the q=3 surface is rotating much more slowly than the core, as it is at fairly large minor radius when it first enters due to the strong reversed shear and peaked rotation profile. The red curve shows the frequency of the dominant low-frequency n=1 mode perturbation. The large n=1 mode strikes at t~0.25 s, with a frequency equal to that of the q=3 surface. This mode leads to rapid rotation damping, and the mode and plasma rotation frequencies rapidly go to zero.

This type of disruption, with rotating MHD modes that slow and lock to the wall, is among the most common for early flat-top disruptions. When discharges disrupt in this fashion, the most common control room response is to modify the early gas fuelling. This change does not necessarily eliminate the mode, but the locking to the wall can typically be avoided.

An example of this behavior is given in Fig. 15, where a discharge taken shortly after that in Fig. 14 is illustrated. In this case, the discharge in Fig. 14 was fueled using supersonic gas injector [145] located on the low-field side of the device, while that in Fig.15 used high-field side fueling [146], entering the plasma at about 70 ms. We note, however, that similar sensitivity has been observed to changes in the amount of gas injected from the high-field side. Fig 15a) shows the spectrogram for the second discharge, while Figs. 15b) through 15g) show a comparison of some characteristic waveforms between the two discharges under discussion.
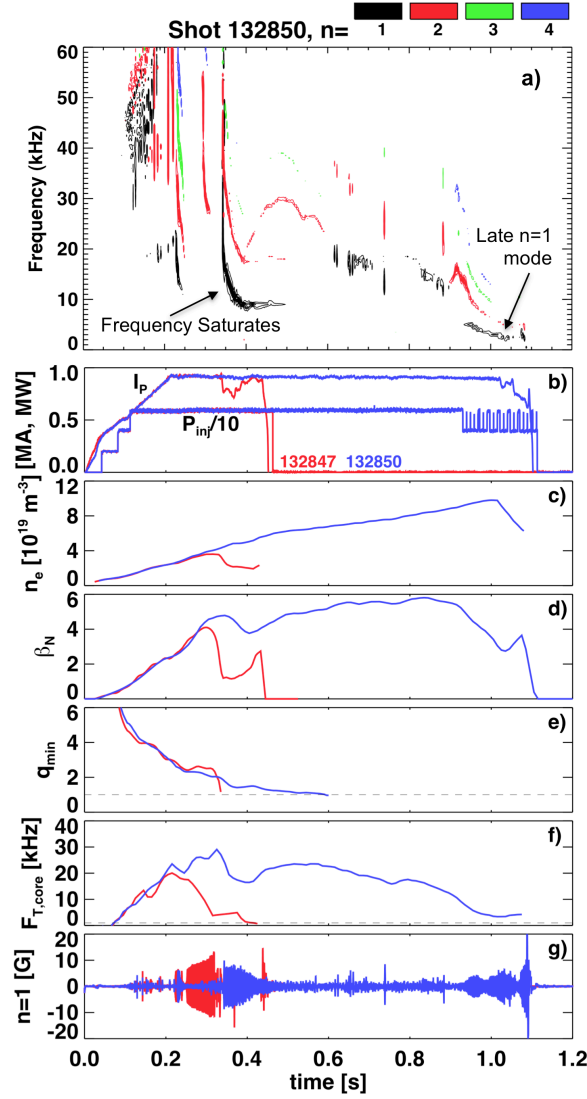
Fig. 15: a) Spectrogram for a discharge that avoids an early disruption through modification of the gas fuelling. Also shown are comparisons of b) the plasma current and heating power, c) the line average density, d) the normalized β, e) the minimum safety factor, f) the core toroidal rotation, and g) the n=1 MHD activity, for the stable discharge (132850) and the unstable discharge in Fig. 14.

Considering Fig. 15a) first, we see that the early MHD modes are not eliminated in the second discharge. However, their frequency evolution is modified, and no mode frequency drops beneath 10 kHz; this is sufficient to prevent the disruption. Fig 15b) illustrates that the current ramp and injected power are similar, while Figs. 15c)-15e) shows that the evolution of the line average density, β_N, and q_{min} are also similar until the large mode strikes at t=0.25 s in discharge 132847. Fig. 15f) illustrates the rapid rotation damping associated with that mode. Note that the more successful discharge (132850) also has a large mode at t=0.38 seconds, resulting in substantial rotation damping. However, the discharge is able to survive this damping and enter a high-performance phase.

23

The exact details of how the early gas fuelling impacts the mode stability and rotation damping has not been established. A reasonable hypothesis is that the gas fuelling changes result in small modifications to the edge temperature, and thus resistivity. There may also be changes in the characteristics of the early chirping modes that are visible at greater than 30 kHz is Figs. 14a) and 15a); these may change the fast ion current profile. These two effects in turn impact the radius of and magnetic shear at the rational surfaces when they enter the plasma, which can impact the amplitude and spatial distribution of MHD instabilities that form. However, the detailed MHD calculations required to validate this hypothesis have not been attempted.

Finally, we note that discharge 132850 has a second n=1 mode that grows starting at t~0.93 s. This mode results in a substantial reduction in β_N, and large rotation damping. The impact of this type of n=1 mode on the safe operating space will be discussed in Section 8.
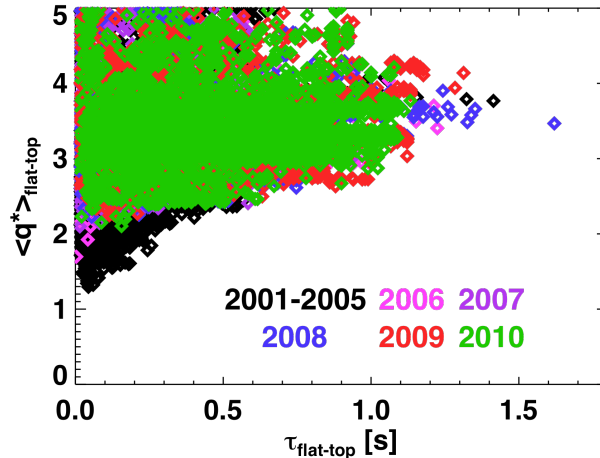
7: Disruption causes at the low-q* boundary

Fig. 16: The flat-top average of q, plotted against the flat-top duration, for the complete NSTX database.*

We begin this section by examining Fig. 16, which shows the value of q* averaged over the I_P flat-top, as a function of the I_P flat-top duration. Here, the I_P flat-top is defined as all times in the discharge where I_P is greater than 85% of the maximum value. The colors are indicative of the year during which the discharge occurred, with black points corresponding to earlier NSTX operation that is not included in the disruptivity analysis in sections 4 & 5.

First, note that NSTX operation at very low q* has been achieved, with values as low as q*=1.3 recorded in the database. However, these discharges are extremely short, often with essentially no recognizable flat-top. This confirms that the NSTX data-set is at least consistent with the idea of a "hard" MHD stability limit at q*~1.3, as anticipated from ideal MHD theory. The pulse durations increase significantly as q* is then raised, with pulses of ~1 second duration occurring for q*>~2.7.

We also see that operation at very low values of q* was most common in the early years of NSTX operations. Those campaigns had significant run time dedicated to achieving very high toroidal β values, which, by Troyon scaling, are best achieved at higher I_P/B_T, and thus low q*. High values of $β_T$ were achieved [13,147], but for only very short duration. In later years of NSTX, more emphasis has been placed on achieving sustained high values of the non-inductive fraction [103,125,148,149] or $β_N$ [78,109,111]. As a consequence, there were few or no attempts to access this very low q* regime during the run campaigns used for disruptivity analysis in section 4.

Hence, while we find that while equilibria with q* as low as 1.3 have been transiently generated, we find an *operational* disruptive q* limit roughly defined by q*<2.5. We have examined a number of these disruptions at the operational low-q boundary during the 2005-2010 campaign, and indicate some of the disruption causes below.

o   The early rotating MHD modes described in the previous section are a significant source of disruptivity at low q*. We observe many instances of these modes locking to the wall and leading to disruption. Additionally, we observe many cases where the rotation braking associated with these modes apparently leads to onset of subsequent disruptive instabilities. It is clear that optimization of the current ramp phase of the discharge is especially important for achieving reliable operation at low-q*.

o   It has been documented that the L->H threshold power in NSTX has positive scaling with plasma current [150-152], unlike the widely accepted conventional aspect ratio scaling $P_{LH} = 0.0488 n_{e20}^{0.72} B_T^{0.8} S_A^{0.94}$ [153]. This results in a significant fraction of high-current discharges failing to reach H-mode, or succumbing to H->L back transitions early in the discharge. These discharges typically then disrupt at fairly low $β_N$, due the reduced stability of configurations with high values of the pressure peaking factor (see Fig. 9 & 12).

o   NSTX has observed an improved confinement mode known as the enhanced pedestal H-mode (EPH-mode) [154]. In most EPH cases, the discharge transitions to H-mode in the standard way; an ELM then follows triggering the transition to the EPH configuration. The occurrence of these confinement transition increases at higher plasma current, or low q*. However, these low-q EPH scenarios are typically short lived, resulting in disruption soon after the confinement transition [155]. The exact cause of these disruptions in EPH modes is under investigation.

o   Finally, an additional cause of disruption at low q* is the onset of core n=1 MHD activity as the central safety factor approaches unity. These modes can onset at any value of q_{95} if q_{min} becomes low enough. However, the large inductive component at high current more often leads to the rapid onset of these modes, which are the subject of the next section.
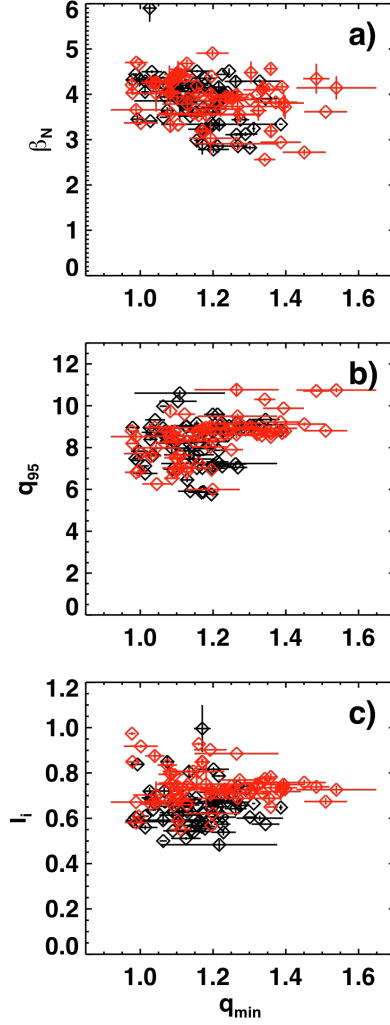
Fig. 17: Values of q_{min} at core n=1 mode onset, plotted again a) β_N, b) q_{95}, and c) l_i. Red symbols are for triggered modes, while black cases are for modes that onset without a clear trigger.

8: Onset of core n=1 activity

The previous sections noted that long-lived core n=1 modes, rotating with the plasma, often occur in NSTX. These modes were first documented in Refs. [123,124], where it was shown that the modes had a large m/n=1/1 core kink component. They were shown to be responsible for the redistribution of fast ions and braking of the plasma rotation. Various saturation mechanisms for the mode were discussed.

Refs. [73,74] studied a class of m/n=2/1 magnetic islands, and showed that they had many characteristics of 2/1 neoclassical tearing mode. Ref. [73] showed that these modes could be triggered by energetic particle modes (EPMs) [156] or edge localized modes (ELMs) [157], or grow without any obvious trigger, and that their onset was correlated with rotation shear at the q=2 surface. It was also noted that there was often a large 1/1 core kink present simultaneously with the island. This coupled 2/1+1/1 mode was reconstructed from soft X-ray emission data in Refs [103,125], and its impact on the

core plasma was discussed in Ref. [103]. See refs. [103,123-125] for additional information on the impact of these modes on NSTX plasmas.

These NSTX modes were studied numerically with the PEST-1 [158] and M3D [159] codes in Ref. [160]. It was shown that these modes became linearly unstable as q_{min} approached 1. Non-linearly saturated states with both 1/1 ideal displacements and 2/1 magnetic islands were observed.

In the context of the present work, the question is to understand how these instabilities constrain the "safe" operating regime in NSTX. To this end, a database of 138 discharges with these core MHD modes has been formed, using data from the 2008-2010 operating campaigns. These discharges have had their equilibrium calculated with the LRDFIT equilibrium reconstruction code [124]; these reconstructions are constrained by external magnetics and coil currents, pitch angle data from a motional Stark effect diagnostic [161], and the requirement that the magnetic surfaces be isotherms. The database records various equilibrium properties at time at mode onset (q_{min}, q_0, β_N, l_i,…), the plasma rotation frequency at the q=2 surface, and the initial mode frequency.

Also recorded in the database is information about the various trigger types, indicated by the symbol colors in Fig 17. Triggerless cases are indicated in black; these discharges show the n=1 Mirnov coil amplitude growing smoothly from the background without any clear triggering disturbances. Cases with various triggering perturbations are shown in red. The ELM triggered cases have a clear ELM at the time of the n=1 mode onset, and typically show the mode frequency sweeping up from slower than the q=2 rotation at trigger time, to being equal to the q=2 rotation frequency some tens of milliseconds later. The EPM triggered cases show a clear high-frequency burst at the time of the mode onset, as well as a rapid drop in the neutron emission. Finally, there are a small fraction of cases in the "triggered" category where EPMs and/or ELMs are present, but it is not possible to correlate the mode onset with any individual event.

The values of q_{min} at mode onset are shown in Fig. 17 a-c), plotted against various other equilibrium parameters. Fig 17a) shows that these modes can onset over a wide range of β_N, from values around 2.75 to greater than 5.0. This spans from well under the no-wall β_N limit, to well above that limit. The range of q_{min} at mode onset, however, is fairly restricted, with almost all modes striking with $1.0 < q_{min} < 1.25$. Fig. 17b) shows the values of q_{95} and q_{min} at mode onset. We see that while the range of q_{min} is rather restricted, the values of q_{95} range from 6 up to 11. Finally, Fig. 17c) shows that values of q_{min} and l_i at mode onset; we choose this because l_i was previously shown to be a rough indicator of tearing onset the ITER-similarity discharges in DIII-D [162]. In this case, however, the modes onset with a very broad range of l_i values, ranging from 0.5 all the way to 1.0. From these studies, we infer that q_{min} is the best single parameter indicator of the mode onset conditions.
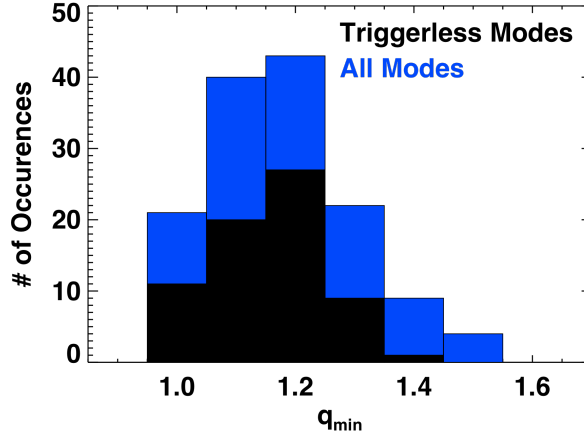
Fig. 18: Histogram of the values of q_{min} at the time of core n=1 mode onset, for the full 138 discharge database, and for the discharge subset with no clear trigger.

A histogram of the q_{min} values at mode onset is shown in Fig. 18. The complete data set is plotted in blue, as well as a subset for those cases in which the modes onset in otherwise quiescent phases with no clear triggering disturbance. For the complete data set, we see a strong peak in occurrences for $1.0 < q_{min} < 1.3$, with values trailing off to values as high as 1.5. We note that this explains part of the reduction of disruptivity with power and β_N, as increasing these variables will tend to raise the bootstrap current, which contributes to raising q_{min}. Furthermore, the slowed current evolution with higher power and β_N will delay the approach to unstable q_{min} values.

The triggerless cases are restricted to somewhat lower values of q_{min} though values up to $q_{min}=1.4$ have been observed. The peak of the histogram is located in the vicinity of 1.1 to 1.2. At these low q_{min} values, it appears that the ideal MHD onset mechanisms for the m/n = 1/1 modes discussed in Refs. [160,163,164] are likely at play. For the few triggerless cases at higher q_{min} it is possible that there is some trigger mechanism not observable in the data.

The details of the mode physics, however, are not the purpose of the present paper, which is interested in determining regions of safe operations windows. From these figures, we infer that operations with q_{min} beneath ~1.25 will likely be prone to core n=1 MHD modes. If the spectrum of disturbances from ELMs and EPMs (and possibly other perturbations as well) is eliminated, then operation with q_{min} not significantly above 1.3 may be acceptable. On the other hand, if these perturbations are not eliminated, then operation with $q_{min}>1.5$ may be more appropriate. We also note in passing that EPMs have previously been implicated in the triggering of NTMs in ASDEX-Upgrade [165] and RWMs in DIII-D and JT-60 [166]. Similarly, ELMs have been indicated in the triggering of the dangerous 2/1 NTM in DIII-D [167] and JET [168], RWMs in DIII-D [80], and core n=1 kink modes in JET [169]. Hence, we conclude that the sensitivity of the global stability to nominally small perturbations is not a feature unique to the ST.

In the context of disruptivity, these modes do not typically lead to prompt disruption. Rather, as indicated in Refs [103,123,124], or Fig. 15, these modes typically

grow to fairly large amplitude over a period of 10s of milliseconds, during which time they can be easily detected. The sole exception to this statement are the modes triggered by EPMs, which, as inferred from the Mirnov sensor signal, can be struck at fairly large amplitude. Once the mode becomes large, it begins to damp the plasma rotation, another easily detectable mode signature. It is only when the plasma rotation drops sufficiently for the mode to lock to the wall does the disruption typically occur. Thus, there should be sufficient time before a disruption to detect the mode and instigate some mitigating control response. The details of an appropriate control response are beyond the scope of the present work.

We also wish to note that a similar n=1 core mode has been observed in MAST [163,164]. These modes are similar in that they have strong m/n =1/1 components that onset as q_{min} approaches unity. However, those modes in MAST are distinguished by a lack of any measurable reconnection and island formation, and their onset frequency is close to that core rotation frequency. As described in Refs [73,103,125], the NSTX modes do have a tearing component, and their frequency is a better match to the rotation at the q=2 surface. Hence, while these modes may share some similarities with those observed in MAST, they also have significant differences.

Finally we wish to note that although operation with $q_{min}<\sim1.2$ is clearly more prone to the onset of these modes, many examples exist with long durations of operation with q_{min} in this ostensibly dangerous range, and without these modes striking. An example pair of such discharges is shown in Fig. 19; note that discharge 129125 was previously discussed in Ref. [78,103], while discharge 135445 was previously discussed in Ref. [103,125].

Fig 19a) shows that these 700 & 750 kA discharges last for up to 1.5 seconds, corresponding to 5-7 current relaxation times. They operate at high values of β_N and q*, the latter due to both the somewhat low current values and the high elongations (not shown). Fig. 19d) shows that the central safety factor hovers just above unity for at least 1 second in these discharges. However, Fig. 19e) shows that except for the start-up MHD activity around 0.25 s, these discharges are free of rotating n=1 MHD. Contributing factors to the observed stability are the lack of ELMs and EPMs in these lithium-conditioned discharges. However, further research is required to demonstrate in detail which equilibrium properties render these types of discharges immune to the "triggerless onset" n=1 modes.
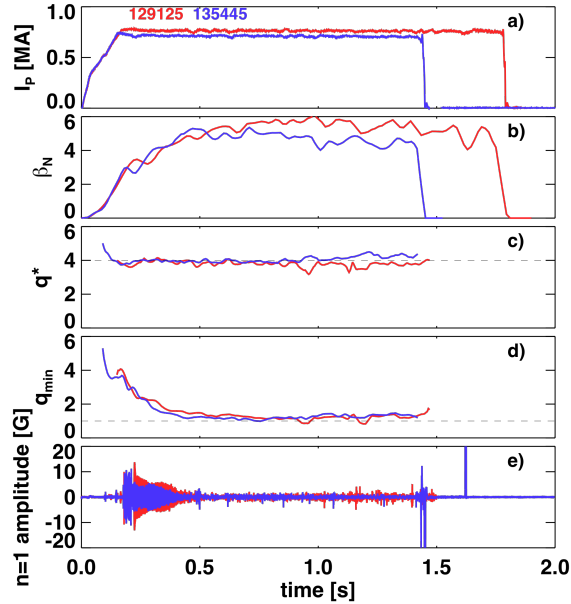
Fig. 19: Time evolution of a) the plasma current, b) the normalized β, c) q*, d) the minimum safety factor, and e) the low frequency rotating n=1 MHD detector. The two discharges selected are among the longest ever achieved in NSTX.

9: Disruptions with the largest stored energy

It was noted in Section 3 that the largest stored energy disruptions typically occur during the plasma current rampdown. This section describes the phenomenology of those disruptions in more detail.

An example large stored-energy disruption during the ramp-down is shown in Fig. 20. As shown in Fig. 20a), this is a 1.1 MA discharge heated by 4 MW of neutral beams. This discharge is operating stably until the solenoid reaches its I_{OH}=-24 kA current limit at t=862 ms. At this time, the solenoid current is ramped back to zero by the power supply control software, applying a very large negative loop voltage to the plasma (see Fig. 20b). This initiates a rapid ramp-down of the plasma current; the current profile changes associated with this ramp-down presumably lead to the very rapid disruption at t~870 ms. Fig. 20c) indicates that the stored energy at the time of disruption was ~320 kJ.

In order to understand the time-scales and dynamics for this disruptions, we examine the neutron and soft X-ray emission; these are shown separately in Fig. 20d) and 20e) respectively, and for a time-window localized to the thermal quench in Fig. 20f). The neutron emission is dominated by beam-target reactions, and so is a good proxy for the fast particle content. We see that this emission drops in two steps. The soft X-ray emission is measured with a pin-hole camera through 100 mm beryllium filters [170]; these filters are the thickest available in the NSTX arrays and generally result in the detected X-rays being localized toward the plasma core. The two separate phases of the thermal quench are readily discernable in the USXR emission. The first rapid energy loss

phase has a duration of roughly 40-60 μs, while the second energy loss phase has a duration of ~200 μs; these two phase are separated by a duration of 1500 μs. Note that the typical Alfven times $\tau_A = 2\pi R_0 / V_A$ are 2-8μs, and it is clear that at least the first of these collapses occur on an Alfvenic time-scale.
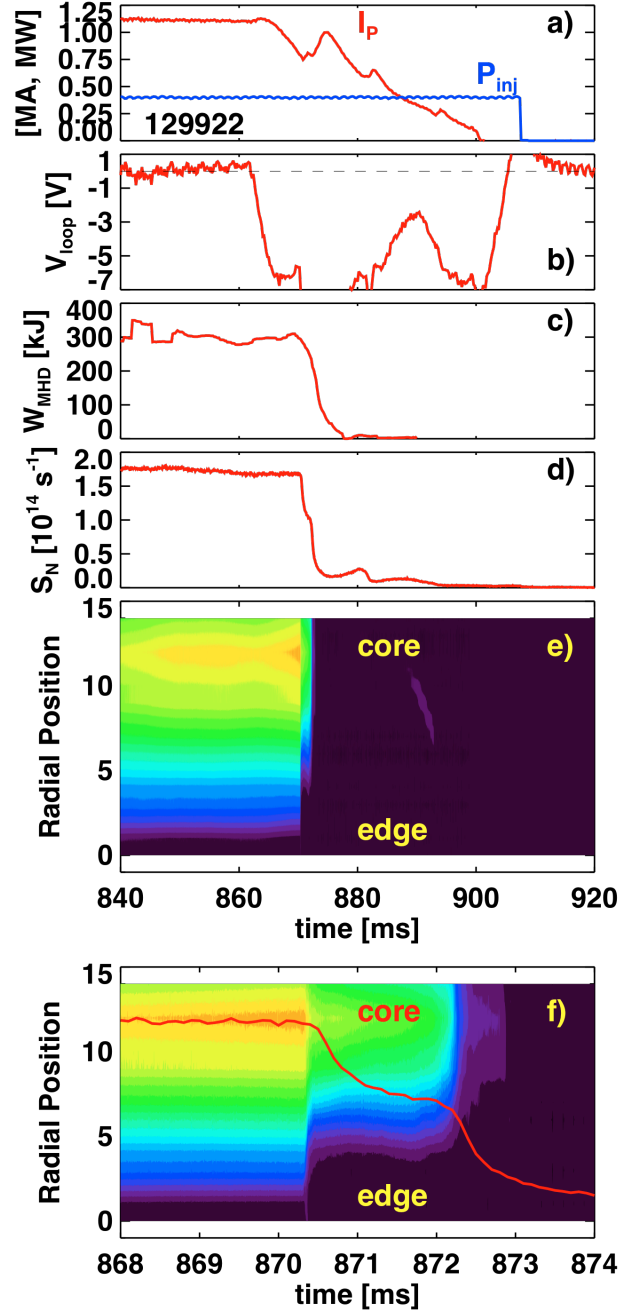

Fig. 20: Time evolution of various quantities during the thermal quench of a large stored energy disruption. Shown are the a) the plasma current and heating power, b) the loop voltage, c) the stored energy, d) the neutron emission, e) contours of soft X-ray emission, and f) the same soft X-ray emission isolating a narrow window during the thermal quench. Also shown in frame f) is a scaled version of the neutron emission.

This type of disruption, initiated by loop-voltage reversal, is responsible for 21 of the 22 largest stored energy disruptions, and all but one of the disruptions with stored energy greater than 275 kJ, in NSTX during the time under consideration. We note that while this disruption was caused by incorrect initiation of the plasma current ramp-down, it clearly shows that such large W_{MHD} disruptions are possible, for instance, in the case of failure of a current drive actuator, and accounting for them should be part of the design of next-step STs.

10: Summary and Implications for Next Step Devices.

This paper has documented the following significant points with regard to disruptivity in high-β NSTX plasmas.

- The disruption rate in NSTX is rather high, with only about 25% of discharges reaching a ramp-down phase (Section 3).
- There is often a significant loss of plasma current and stored energy in the phase following an MHD mode but proceeding the disruptions (Section 3).
- The disruptivity of NSTX plasmas is independent of, or even decreases with, the normalized-β (sects 4 & 5).
- The disruptivity increases rapidly for q*<2.7. This is well above the ideal MHD low-q limit, and is instead related to various operational issues that occur at higher current (Sections 4 & 7).
- Strong shaping and broad current and pressure profiles are critical in reducing the disruptivity (Section 4).
- The disruptivity increases considerably when the core rotation drops beneath ~8kHz, corresponding to $F_{T,core}/F_A < 0.04$ (Section 4).
- Use of n=1 dynamic error field correction and resistive wall mode control results in a significant decrease in the disruptivity (Section 5).
- There are a class of early flat-top disruptions due to MHD modes that develop at rational surfaces where they enter the plasma. The disruption results when these modes brake the plasma rotation sufficiently that the plasma rotation is stopped. The key to avoiding these disruptions has not been not to avoid the MHD modes altogether. Rather, it is important to arrange the early discharge evolution so that the rotation damping is less severe (Section 6).
- In otherwise quiescent discharges, core n=1 modes often grow when q_{min} drops below 1.25. When disturbances such and ELMs or EPMs are present, these n=1 modes can be triggered at q_{min} as high as 1.5 (Section 8).
- The largest stored-energy disruptions occur when the loop voltage is reversed at full current and heating power. These show a two-part thermal quench, with the time-scales of a few tens of Alfven times (section 9).

With regard to next-step spherical torus devices, the implications are rather obvious. The equilibria likely should be strongly shaped, consistent with robust vertical

stability and boundary control. The current drive actuators should be arranged to provide a broad current profile. This is of course the natural result in the case of the bootstrap current. However, many next-step ST designs rely on neutral beam current drive, and those neutral beams should be configured to elevate q_{min} sufficiently above one that these core n=1 modes can be avoided. Furthermore, it appears that internal transport barrier scenarios may be less desirable, due to the increased disruptivity as the pressure peaking is increased. Transients that could destabilize MHD modes or result in the loss of boundary control should be avoided. Robust current ramp-down and soft landing strategies should be developed.

Much of the research required to meet these requirements will be carried out in the 2 MA class upgrades to existing STs. These are, in the United States, NSTX-Upgrade [134,171], and in the UK, MAST-Upgrade [172]. Both devices will have great flexibility to control the central safety factor by varying the density, current, and neutral beam selection, allowing the optimal value of q_{min} to be better determined. The upgraded magnet capabilities will allow disruption avoidance studies in the I_P flat-top for 20-30 current relaxation times [134] in NSTX-Upgrade. This will provide an important test of error field reduction, RWM avoidance, current profile maintenance, and boundary control, all with the goal of eliminating flat-top disruptions. However, it is clear that better control of both the current ramp-up and early flat-top, and the discharge termination phase, will be required to fully exploit the capabilities of that upgrade. With regard to the ramp-up, the significantly larger solenoid current and heating capability in NSTX-U may allow the plasma current to be ramped up more slowly than is shown in Figs 14 & 15. This may in turn provide an additional degree of freedom in understanding and avoiding those deleterious modes that occur during the current ramp-up.

10: Acknowledgements

References

[1] "ITER Physics Basis", Nuclear Fusion **39**, 2137 (1999).

[2] V. Riccardo, et al., Plasma Phys. Control Fusion **44**, 905 (2002).

[3] V. Riccardo, A. Loarte, and JET EFDA Contributors, Nuclear Fusion **45**, 1427 (2005).

[4] G. Federici, Phys. Scr. **T124**, 1 (2006).

[5] A. Loarte, et al., Phys. Scr. **T128**, 222 (2007).

[6] T.C. Hender, et al., Nuclear Fusion **47**, S128 (2007).

[7] G. Arnoux, et al., Nuclear Fusion **49**, 085038 (2008).

[8] V Riccardo, et al., Plasma Phys. Control. Fusion **52**, 024018 (2010).

[9] D.A. Humphreys and D.G. Whyte, Phys. Plasmas **7**, 4057 (2000).

[10] V. Riccardo, P. Barabaschi, and M. Sugihara, Plasma Phys. Control. Fusion **47**, 117 (2005).

[11] J.C. Wesley, et al., Disruption Characterization and Database Activities for ITER, paper IT/P1-21, IAEA FEC, Chengdu China (2006)

[12] S.P. Gerhardt, J. E. Menard, and the NSTX Team, Nuclear Fusion **49**, 025005 (2009).

[13] J.C. Wesley, et al., "Disruption, Halo Current and Rapid Shutdown Database Activities for ITER", paper ITR/P1-26, IAEA FEC, Deajeon, Korea (2010).

[14] Y. Shibata , et al, Nuclear Fusion **50**, 025012 (2010).

[15] M. Sugihara, et al., Nuclear Fusion **47**, 337 (2007).

[16] M.N. Rosenbluth and S.V. Putvinski, Nuclear Fusion **37**, 1355 (1997).

[17] R. Yoshino , S. Tokuda and Y. Kawano, Nuclear Fusion **39**, 151 (1999).

[18] R. Yoshino , and S. Tokuda, Nuclear Fusion **40**, 1293 (2000).

[19] R.D. Gill , et al., Nuclear Fusion **42**, 1039 (2002).

[20] H. Tamai, et al., Nuclear Fusion **42**, 290 (2002).

[21] M. Forster, et al., Nuclear Fusion **51**, 043003 (2011).

[22] V. Sizyuk and A. Hassanein, Nuclear Fusion **49**, 095003 (2009).

[23] E. A. Lazarus, et al., Phys. Fluids **3**, 2220 (1991).

[24] F. Hofmann , M.J. Dutch , D.J. Ward , M. Anton , I. Furno , J.B. Lister and J.-M. Moret, Nuclear Fusion **37**, 681 (1997).

[25] F. Hofmann , A. Favre , P.-F. Isoz , Y. Martin , J.-M. Moret and C. Nieswand, Nuclear Fusion **40**, 767 (2000).

[26] C.E. Kessel, P. Heitzenroeder and C. Jun, Nuclear Fusion **41**, 953 (2001).

[27] D.A. Humphreys , et al., Nuclear Fusion **49**, 115003 (2009).

[28] E. J. Strait, L.L Lao, J.L. Luxon, and E.E. Reis, Nuclear Fusion **31**, 527 (1991).

[29] R. S. Granetz, et al., Nuclear Fusion **36**, 545 (1996).

[30] Y. Neyatani, R. Yoshino, Y. Nakamura, and S. Sakurai, Nuclear Fusion **39**, 559 (1999).

[31] G. F. Counsell, et al., Plasma Phys. Control. Fusion **49**, 435 (2007).

[32] V. Riccardo, et al., Nuclear Fusion **49**, 055012 (2009).

[33] G. Pautasso, et al., Nuclear Fusion **51**, 043010 (2011).

[34] S.P. Gerhardt, et al., Nuclear Fusion **52**, 063005 (2012).

[35] P.C. De Vries, et al, Nuclear Fusion **51**, 053018 (2011).

[36] F. Troyon, et al., Plasma Phys. Control. Fusion **26**, 209 (1984).

[37] J.E. Menard, et al., Nuclear Fusion **37**, 595 (1997).

[38] R. L. Miller, et al., Phys. Plasmas **4**, 1062 (1997).

[39] E. J. Strait, Phys. Plasmas **1**, 1415 (1994).

[40] A. Turnbull, et al., Phys. Plasmas **6**, 1113 (1999).

[41] W. Howl, et al., Phys. Fluids B **4**, 1724 (1992).

[42] A. Bondeson and D.J. Ward, Phys. Rev. Lett **72**. 2709 (1994).

[43] D.J. Ward and A. Bondeson, Phys. Plasmas **2**, 1570 (1995).

[44] E.J. Strait, et al., Nuclear Fusion **39**, 1977 (1999).

[45] A.M. Garofalo, et al., Phys. Plasmas **6**, 1893 (1999).

[46] S.A. Sabbagh, et al., Phys. Plasmas 9, 2085 (2002).

[47] S.A. Sabbagh, et al., Nuclear Fusion 44, 560 (2004)

[48] A.C. Sontag, et al., Phys. Plasmas **12**, 056112 (2005).

[49] S.A. Sabbagh, et al., Nuclear Fusion **46**, 635 (2006).

[50] A.C. Sontag, et al., Nuclear Fusion **47**, 1005 (2007).

[51] E. J. Strait, et al., Phys. Plasmas **11**, 2505 (2004).

[52] S.A. Sabbagh, et al., Phys. Rev. Lett. 97, 045004 (2006).

[53] J. E. Menard, et al., Phys. Plasmas **11**, 639 (2004).

[54] J.A. Wesson, et al., Nuclear Fusion **29**, 641 (1989).

[55] S.M. Kaye, et al, Nuclear Fusion **28**, 19

[56] P.C. de Vries, M.F. Johnson, I. Segui and JET EFDA Contributors, nuclear Fusion **49**, 055011 (2009).

[57] M. Shimada, et al., Nuclear Fusion **47**, S1 (2007).

[58] M. Murakami, et al., Nuclear Fusion **16**, 347 (1976).

[59] M. Greenwald, et al., Nuclear Fusion **28**, 2199 (1988).

[60] R. Maingi, et al., Phys. Plasmas **4**, 1752 (1997).

[61] M. Greenwald, et al, Plasma Phys. Control. Fusion **44**, R27 (2002).

[62] D.A. Gates, et al., Phys. Rev. Lett **108**, 165001 (2012).

[63] F. Wagner, et al., Phys. Rev. Lett. **49**, 1408 (1982).

[64] P. H. Rebut and M. Hugon, Plasma Physics and Controlled Nuclear Fusion Research 1984: Proc. 10th Int. Conf. London, 1984 (IAEA, Vienna, 1985), Vol. 2.

[65] W. Suttrop et al., Nuclear Fusion **37**, 119 (1997)

[66] F. Salzedas, et al., Phys. Rev. Lett **88**, 075002 (2002).

[67] Z. Chang, et al., Phys. Rev. Lett. **74**, 4663 (1995).

[68] R.J. La Haye, et al, Nuclear Fusion **37**, 397 (1997).

[69] H. Zohm, et al., Plasma Phys. Control. Fusion **39**, B237 (1997).

[70] O. Sauter, et al, Phys. Plasmas **4**, 1654 (1997).

[71] D. A. Gates, et al., Nuclear Fusion **37**, 1593 (1997).

[72] R. J. La Haye, et al, Phys. Plamas **13**, 055501 (2006).

[73] S.P. Gerhardt, et al., Nuclear Fusion **49**, 032003 (2009)
[74] R. J. La Haye, et al., Phys. Plasmas **19**, 062506 (2012).

[75] R. Buttery, et al., Phys. Rev. Lett. **88**, 125005 (2002).

[76] K.J. Gibson, et al., Plasma Phys. Control. Fusion **52**, 124041 (2010).

[77] A. M. Garofalo, R. J. LaHaye, and J.T. Scoville, Nuclear Fusion **42**, 1335 (2002).

[78] J.E. Menard, et al., Nuclear Fusion **50**, 045008 (2010).

[79] M. Okabayashi, et al., Nuclear Fusion **45**, 1715 (2005).

[80] A.M. Garofalo, et al., Nuclear Fusion **47**, 1121 (2007).

[81] M. Okabayashi, et al., Nuclear Fusion **49**, 125003 (2009).

[82] G. Gantenbein, et al., Phys. Rev. Lett. **85**, 1242 (2000).

[83] A. Isayama, et al., Plasma Phys. Control. Fusion **42**, L37 (2000).

[84] C. C. Petty, et al., Nuclear Fusion **44**, 243 (2004).

[85] M. Maraschek, et al., Nuclear Fusion **45**, 1369 (2005).

[86] D.A. Humphreys, et al, Phys. Plasmas **13**, 056113 (2006)

[87] R.J. La Haye, et al, Nuclear Fusion **45**, L37 (2005)

[88] M. Abdou, Fusion Eng. And Design **27**, 111 (1995).
[89] Y-K M Peng, et al., Plasma Phys. Control. Fusion **47**, B263 (2005).

[90] H.R Wilson, et al., *A Steady State Spherical Tokamak for Components Testing*,

   IAEA Fusion Energy Conference, Paper FT/3-1Ra, Villamoura, Portugal (2004).

[91] G.M. Voss, et al., Fusion Eng. and Design **83**, 1648 (2008).

[92] Y-K M Peng, et al., *Effects of Physics Conservatism and Aspect Ratio on Remote Handling for Compact Component Test Facilities (CTFs)*, Paper FT/P3-14, Geneva (2008).

[93] Y-K M Peng, et al, Fusion Science and Technology **56**, 957 (2009)

[94] Y-K M Peng, et al., *Fusion Nuclear Science Facility (FNSF) before Upgrade to Component Test Facility (CTF),* Paper FT/P2-Ra, Daejon (2010).

[95] R.D. Stambaugh, et al., *Candidates for a Fusion Nuclear Science Facility (FDF and ST-CTF),* Paper P2.110, 37th EPS Conference on Plasma Physics, Dublin, Ireland (2010).

[96] M. Ono, et al. Nuclear Fusion **40**, 557 (2000)

[97] T. Stevenson, et al., A neutral beam injector upgrade for NSTX, PPPL Report 3651 (2002).

[98] S.P. Gerhardt, et al., Fusion Sci. and Tech. **61**, 11 (2012).

[99] J. R. Wilson, et al., Phys. Plasmas **10**, 1733 (2003).

[100] L. L. Lao, Nuclear Fusion **25**, 1611 (1985).

[101] S.A. Sabbagh, et al., Nuclear Fusion 41, 1601 (2001).

[102] B. P. LeBlanc, et al., Rev. Sci. Instrum. **74**, 1659 (2003).

[103] S.P. Gerhardt, et al., Nuclear Fusion **51**, 073031 (2011).

[104] R.E. Bell, and R. Feder, Rev. Sci. Instrum. **81**, 10D724 (2010).

[105] R.J. La Haye, et al., Phys. Plasmas **9**, 2051 (2002).

[106] W. Zhu, et al., Phys. Rev. Lett. **96**, 225002 (2006).

[107] A. M. Garofalo, Phys. Rev. Lett. **101**, 195005 (2008).

[108]. J.-K. Park, A. H. Boozer, and J.E. Menard, Phys. Rev. Lett **102**, 065002 (2009).

[109] S.A Sabbagh, et al., Nuclear Fusion **50** (2010) 025020.

[110] A.J. Cole, et al., Phys. Rev. Lett. **106**, 225002 (2011).

[111] S.A. Sabbagh, et al., *Resistive Wall Mode Stabilization and Plasma Rotation Damping Considerations for Maintaining High Beta Plasma Discharges in NSTX,* Paper EXS/5-5, Daejeon (2010).

[112] S.P. Gerhardt, et al., Plasma Phys. Control Fusion **52**, 104003 (2010).

[113] S.P. Gerhardt, et al., Nuclear Fusion **50**, 064015 (2010).

[114] J.M. Canik, et al., Phys. Rev. Lett. **104**, 045001 (2010)

[115] J.M. Canik, et al., Nuclear Fusion **50**, 034012 (2010).

[116] J.M. Canik, et al., Nuclear Fusion **50**, 064016 (2010).

[117] J.R. Ferron, et al., Nuclear Fusion 38, 1055 (1998).

[118] D.A. Gates, et al., Nuclear Fusion 46, 17 (2006).
[119] E. Kolemen, et al, Nuclear Fusion 50, 105010 (2010).

[120] E. Kolemen, et al., Nuclear Fusion 51, 113024 (2011).

[121] H. Kugel, et al., Phys. Plasmas 15, 056118 (2008).

[122] M. G. Bell et al., Plasma Phys Control Fusion **51**, 124054 (2009).

[123] J.E. Menard, et al., Nuclear Fusion **45**, 539 (2005).

[124] J.E. Menard, et al., Phys. Rev. Lett **97**, 095002 (2006).
[125] S.P. Gerhardt, et al., Nuclear Fusion **51**, 033004 (2011).

[126] H.W. Kugel, et al, Fusion Engineering and Design **84**, 1125 (2009).
[127] P.N. Yushmanov, et al., Nuclear Fusion **30**, 1999 (1990)

[128] E. A. Lazarus, et al., Phys. Plasmas B **4**, 3644 (1992).

[129] E. Lazarus, et al., Phys. Rev. Lett **77**, 2714 (1996).

[130] S. A. Sabbagh et al., Proceedings of the 16th International Conference on Fusion Energy, Montreal, CA, 7-11 1996 (1996) AP2-17.

[131] A.C.C Sips, et al., Plasma Phys. Control. Fusion **47**, A19 (2005).

[132] J.R. Ferron, et al., Phys. Plasmas **12**, 056126 (2005).

[133] J.E. Menard, et al., Nuclear Fusion **43**, 330(2003).
[134] S.P. Gerhardt, et al., Nuclear Fusion **52**, 083020 (2012).

[135] H. Reimerdes, et al., Nuclear Fusion **45**, 368 (2005).

[136] H. Reimerdes, et al., Nuclear Fusion **49**, B349 (2007).
[137] D.K Mansfield, et al, Journal of Nuclear Materials **390-391**, 764 (2009).

[138] R. Maingi, et al., Phys. Rev. Lett. **103**, 075001 (2009).

[139] D.P. Boyle, et al., Plasma Phys. Control. Fusion **53**, 105011 (2011).

[140] F. Scotti, et al., Journal of Nuclear Materials **415**, S405 (2011).

[141] A.H. Boozer, Phys. Rev. Lett. **86**, 5059 (2001).

[142] H. Reimerdes, et al., Phys. Rev. Lett. **93**, 135002 (2004).

[143] A. Bortolon, to be submitted to Physics of Plasmas.

[144] W.W. Heidbrink, et al, Nuclear Fusion 43, 883 (2003).

[145] V.A. Sookhanovskii, et al., Rev. Sci. Instrum. **75**, 4320 (2004).

[146] R. Maingi, et al, Plasma Phys. Control. Fusion **46**, A305 (2004).

[147] D. A. Gates, et al., Phys. Plasmas **10**, 1659 (2003).

[148] D. A. Gates, et al., Nuclear Fusion **47**, 1376 (2007).

[149] D. A. Gates, et al., Nuclear Fusion **49**, 104016 (2009).
[150] C. Bush, et al., Phys. Plasmas **10**, 1755 (2003).

[151] R. Maingi, et al, Nuclear Fusion **50**, 064010 (2010).

[152] S.M. Kaye, et al., Nuclear Fusion **51**, 113019 (2011).

[153] Y.R. Martin, et al., J. Phys.: Conf. Ser. **123**, 012033 (2008).

[154] R. Maingi, et al., Phys. Rev. Lett. **105**, 135004 (2010).

[155] R. Maingi et al., J. Nucl. Mater. 390–391, 440 (2009).

[156] E.D. Fredrickson, L Chen, and R. White, Nuclear Fusion **43**, 1258 (2003).

[157] R. Maingi, et al., Nuclear Fusion **45**, 1066 (2005).

[158] R.C. Grimm, J.M. Greene, and J.L Johnson, 1976, *Computation of the magnetohydrodynamic spectrum in axisymmetric toroidal confinement systems* Methods in Computational Physics vol 16, ed J Killeen (New York: Academic) pp 253–80

[159] W. Park, et al., Phys. Plasmas **6**, 1796–803 (1999).

[160] J. Breslau, et al., Nuclear Fusion **51**, 063027 (2011).

[161] F. Levinton and H. Yuh, Rev. Sci. Instrum. 79, 10F522 (2008).

[162] F. Turco, et al, Nuclear Fusion **50**, 095010 (2010).

[162] F. Turco, et al, Nuclear Fusion **50**, 095010 (2010).

[163] I.T. Chapman, et al. Nuclear Fusion **50**, 045007 (2010).

[164] I.T. Chapman, et al., Nuclear Fusion **51**, 073040 (2011).

[165] A. Gude, et al. Nuclear Fusion **39**, 127 (1999).

[166] M. Okabayashi, et al., Phys. Plasmas **18**, 056112 (2011).

[167] R. Buttery, et al., Phys. Plasmas **15**, 056115 (2008).

[168] T.C. Hender, et al., Nuclear Fusion **44**, 788 (2004).

[169] P. Buratti, et al. Nuclear Fusion **52**, 1 (2012).

[170] D. Stutman, et al., Rev. Sci. Instrum. **70**, 572 (1999).
[171] J.E. Menard et al., Nuclear Fusion **52** 083015 (2012)

[172] D. Stork, et al., *The upgrade to the Mega Amp Spherical Tokamak*, paper ICC/P5-06, IAEA FEC 2010. Daejon, Korea.